Biochemistry

pubs.acs.org/biochemistry
Article

Structural Dynamics of the Methyl-Coenzyme M Reductase Active Site Are Influenced by Coenzyme F_{430} Modifications

Marcelo D. Polêto, Kylie D. Allen,* and Justin A. Lemkul*

Cite This: *Biochemistry* 2024, 63, 1783−1794
Read Online

ABSTRACT: Methyl-coenzyme M reductase (MCR) is a central player in methane biogeochemistry, governing methanogenesis and the anaerobic oxidation of methane (AOM) in methanogens and anaerobic methanotrophs (ANME), respectively. The prosthetic group of MCR is coenzyme F_{430}, a nickel-containing tetrahydrocorphin. Several modified versions of F_{430} have been discovered, including the 17^2-methylthio-F_{430} (mtF_{430}) used by ANME-1 MCR. Here, we employ molecular dynamics (MD) simulations to investigate the active site dynamics of MCR from *Methanosarcina acetivorans* and ANME-1 when bound to the canonical F_{430} compared to 17^2-thioether coenzyme F_{430} variants and substrates (methyl-coenzyme M and coenzyme B) for methane formation. Our simulations highlight the importance of the Gln to Val substitution in accommodating the 17^2 methylthio modification in ANME-1 MCR. Modifications at the 17^2 position disrupt the canonical substrate positioning in *M. acetivorans* MCR. However, in some replicates, active site reorganization to maintain substrate positioning suggests that the modified F_{430} variants could be accommodated in a methanogenic MCR. We additionally report the first quantitative estimate of MCR intrinsic electric fields that are pivotal in driving methane formation. Our results suggest that the electric field aligned along the CH_3-S-CoM thioether bond facilitates homolytic bond cleavage, coinciding with the proposed catalytic mechanism. Structural perturbations, however, weaken and misalign these electric fields, emphasizing the importance of the active site structure in maintaining their integrity. In conclusion, our results deepen the understanding of MCR active site dynamics, the enzyme's organizational role in intrinsic electric fields for catalysis, and the interplay between active site structure and electrostatics.

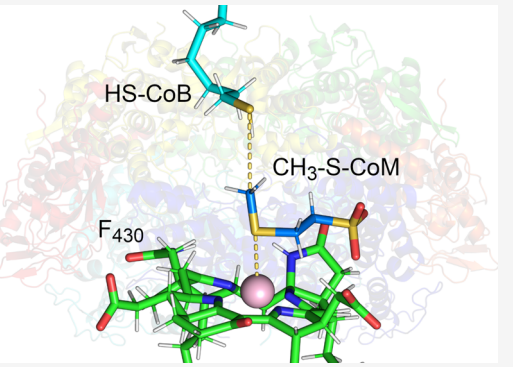

INTRODUCTION

Methanogens are a diverse group of archaea found in a wide range of anaerobic environments including marine and freshwater ecosystems, anaerobic digesters, and animal microbiomes.[1−3] These organisms possess a unique energy metabolism known as methanogenesis, which is responsible for up to 70% of global methane emissions.[4−6] The methane-forming step of methanogenesis is catalyzed by methyl-coenzyme M reductase (MCR), in which methyl-coenzyme M (CH_3-S-CoM) and coenzyme B (HS-CoB) are converted to methane and the CoM-S-S-CoB heterodisulfide (Figure 1A,B).[7] MCR is a dimer of heterotrimers with an $\alpha_2\beta_2\gamma_2$ configuration and two active sites that each harbor the nickel-tetrahydrocorphin prosthetic group, coenzyme F_{430} (Figure 1A).[8] The current working mechanism for MCR catalysis was elucidated from detailed kinetic and spectroscopic experiments[9] and is also supported by several computational studies.[10−13] As shown in Figure 1B, Ni(I) of F_{430} induces homolytic cleavage of the methyl-sulfur bond of CH_3-S-CoM to generate a transient methyl radical and Ni(II)-thiolate. The methyl radical abstracts the hydrogen atom from HS-CoB to produce methane and $^{\bullet}$S-CoB, which reacts with the Ni-bound CoM to generate a disulfide radical anion. One-electron transfer to the Ni then releases the heterodisulfide and regenerates Ni(I).[9] Recently, an alternate binding mode for CH_3-S-CoM has been proposed in which the sulfonate is coordinated to the Ni of F_{430} instead of the thioether.[14] Although the radical mechanism is conserved overall, this orientation would require two steps involving long-range electron transfer through CoM.

Functioning in the reverse direction, MCR also catalyzes the first step in the anaerobic oxidation of methane (AOM) carried out by archaea related to methanogens known as anaerobic methanotrophs (ANME).[15,16] Interestingly, one group of ANME organisms—*Ca.* Methanophagales (ANME-1)—contain a modified form of F_{430} (Figure 1C). The structure was assigned as 17^2-methylthio-F_{430}[17] (hereafter referred to as mtF_{430}), which was later confirmed in the active site of an ANME-1 MCR crystal structure.[18] The F_{430} modification is accommodated by a valine residue (Val419) in place of the

Received: April 1, 2024
Revised: June 13, 2024
Accepted: June 17, 2024
Published: June 24, 2024

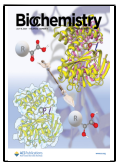

https://doi.org/10.1021/acs.biochem.4c00168
Biochemistry 2024, 63, 1783−1794

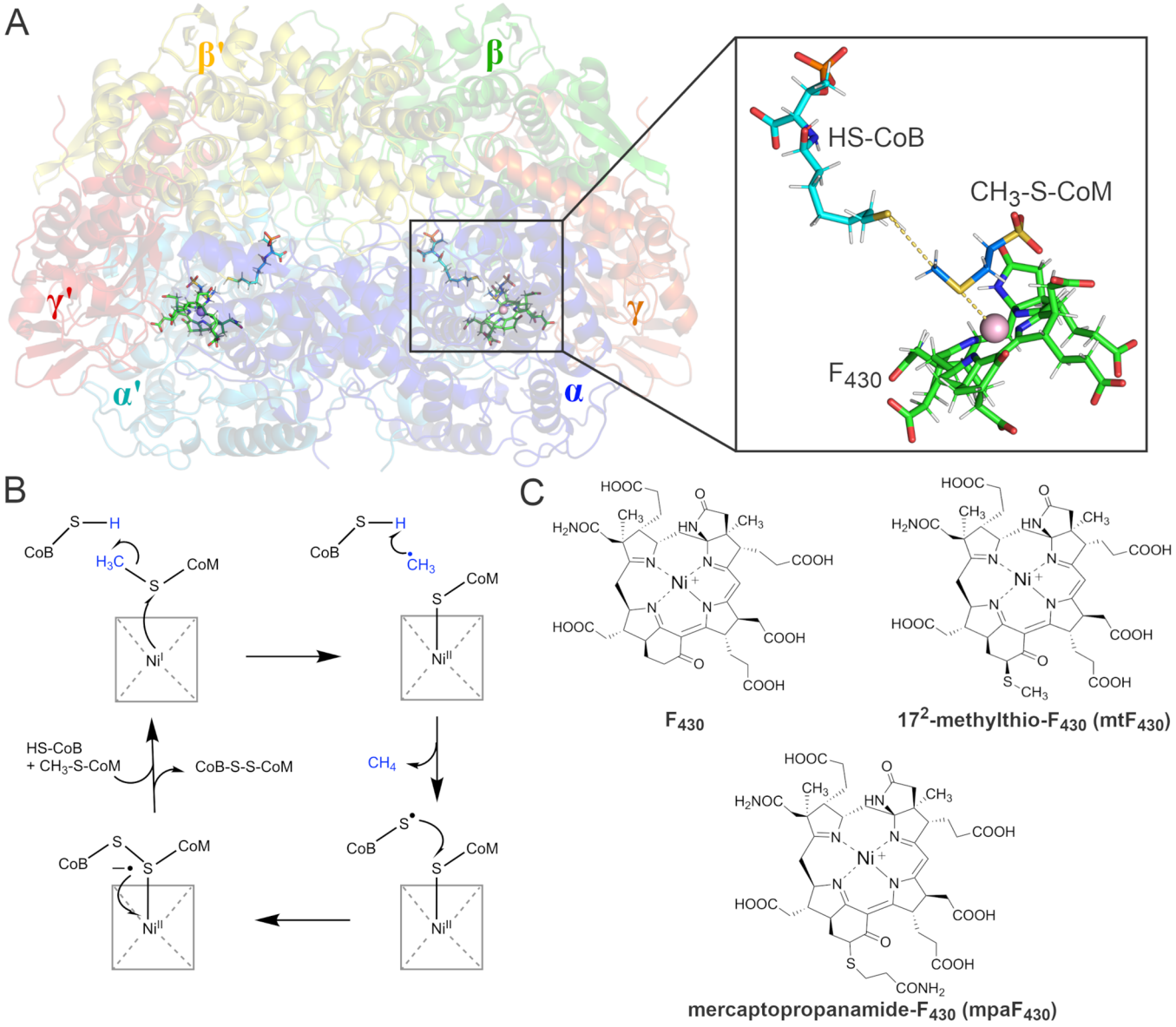

Figure 1. MCR structure and mechanism. (A) Overall structure of MCR from *M. acetivorans*[27] with F_{430} and substrates highlighted in the active site. (B) Working mechanism involving one-electron chemistry with a methyl radical intermediate.[9] (C) Structures of F_{430} variants studied in this work.

corresponding (2-methyl)glutamine residue found in most other MCRs. In addition to mtF_{430}, a handful of modified F_{430}'s were discovered in small-molecule extracts from methanogens[19] and a crystal structure of the MCR homolog in ethane-oxidizing archaea revealed a dimethyl-F_{430} (methyl groups at the 17 and 17^2 positions).[20] The roles of F_{430} modifications with respect to MCR structure and catalysis remain unclear. Recently, computational studies revealed that F_{430}, compared to its biosynthetic precursors, exhibits distinct chemical properties and, thus, reactivity in the methane-forming reaction.[21] Notably, the reduction potential becomes progressively and substantially higher going from early biosynthetic precursors to the final F_{430}, leading to the conclusion that modifications to the macrocyclic ring system have a large impact on the redox properties of the cofactor. Furthermore, the Ni(II)-S bond of F_{430}-Ni(II)-S-CoM was demonstrated to be strongest for F_{430} compared to its precursors, which stabilizes the key transition state promoting CH_3–S bond cleavage (Figure 1B).[21] Thus, additional modifications to F_{430} are expected to influence the reactivity of the cofactor.

The sequences and structures of MCRs from diverse methanogens and ANME are overall highly conserved, especially in the active site region.[8,18,22,23] In Figure 2, we highlight specific residues of interest that will be discussed in this work. Notably, a series of conserved aromatic residues surrounding the thioether bond of CH_3-S-CoM compose what we define as the hydrophobic cage. These residues theoretically provide a microenvironment conducive to radical intermediates, but their specific role in promoting catalysis has not been investigated.

Understanding the details of MCR catalysis will inform the development of methane mitigation strategies as well as biocatalytic/biomimetic approaches to sustainable C–H activation catalysts. Here, we report on extensive molecular dynamics (MD) simulations of MCR. We investigated the

https://doi.org/10.1021/acs.biochem.4c00168
Biochemistry 2024, 63, 1783−1794

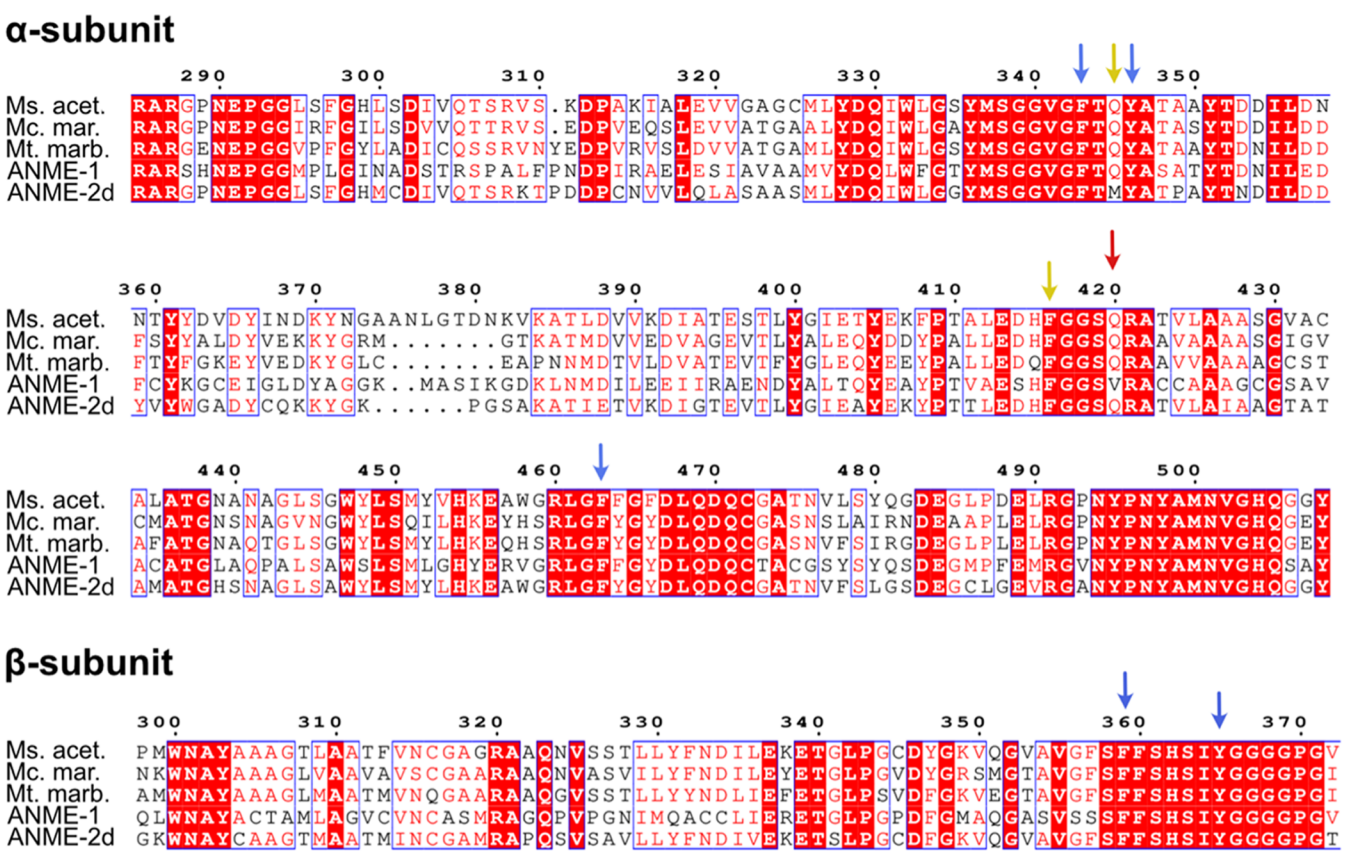

Figure 2. Sequence alignment of selected regions of MCRs from different organisms. Conserved regions are marked in blue boxes. Red arrows mark Gln420 in *M. acetivorans* MCR and Val419 in ANME-1 MCR. Blue arrows mark the positions of Phe and Tyr residues comprising the hydrophobic cage, while yellow arrows mark Phe416 and Gln345 that play a role in positioning modifications at 17^2-position of F_{430} cofactors. Ms. acet. (*Methanosarcina acetivorans*); Mc. mar. (*Methanococcus maripaludis*); Mt. marb. (*Methanothermobacter marburgensis*); ANME-1 (Black Sea Mat ANME-1b, Ca. Methanophagales); ANME-2d (*Methanoperedens nitroreducens*). The alignment was constructed with Clustal Omega[29] and visualized with ESPript.[30]

MCR from a model methanogen, *Methanosarcina acetivorans*, as well as an ANME-1 MCR, in the presence of the canonical F_{430} and two modified versions of F_{430}. Our goal was to describe the active site conformational dynamics and how subtle structural differences among the MCR of each organism could contribute organization of the active site as well as preferences for specific versions of F_{430}. We also investigated the intrinsic electric field driving catalysis in MCR systems to better understand if modification of F_{430} may impact catalysis. Our approach provides new insights into the conformational dynamics of MCR active sites, the relationship between modified F_{430} cofactors and coordination among cofactors, and how MCR is able to organize intrinsic electric fields to facilitate the methane formation reaction.

RESULTS AND DISCUSSION

Initial Simulations to Establish a Starting Structure. The majority of MCR structures solved by X-ray crystallography and available in the Protein Databank, such as entries 5N1Q, 1E6Y, 3POT, 3M2R, and 5A0Y,[22−26] show an electron density between HS-CoM and HS-CoB. In many of these structures, this electron density is modeled as a water molecule trapped inside a hydrophobic cage composed of Phe and Tyr residues surrounding CoM. Considering that the reconstruction of the methyl group of CH_3-S-CoM caused some steric clash with the water molecule, we decided to determine if the presence of water in this location had any structural impact on the active site. To do so, we built a system with *M. acetivorans* MCR[27] that contains the canonical F_{430} (hereafter named *Ma*-F_{430}) including a water molecule in each active site and tracked their dynamics during equilibration and production runs. As shown in Movie S1, the water molecules remained trapped inside the hydrophobic cages throughout equilibration due to the restrained motions of protein atoms but quickly left the active sites once the restraints were released.

As shown in Figure S1, the trapped water molecules left both active sites in all replicates shortly after the unrestrained production run begins. Throughout the 100 ns of simulation in each replicate, no water molecule was able to diffuse inside the hydrophobic cage (assuming a 5-Å cutoff distance from the methyl group of CH_3-S-CoM) or return to its original position as modeled in the crystal structure. These results suggest that a water molecule cannot be located between CH_3-S-CoM and HS-CoB, though the structure obtained via X-ray crystallography contains HS-CoM, not its methylated form. Given the lack of electronic polarization of our model (and thus the inability of water molecules to depolarize in response to their surrounding microenvironments), it is expected that these water molecules in the active site would be repelled in our simulations. However, the strongly hydrophobic nature of the microenvironment suggests that such repulsion would occur even when accounting for more electrostatically robust models. In summary, we could not provide a rationale for possible structural roles for a water molecule in the MCR precatalytic

https://doi.org/10.1021/acs.biochem.4c00168
Biochemistry 2024, 63, 1783−1794

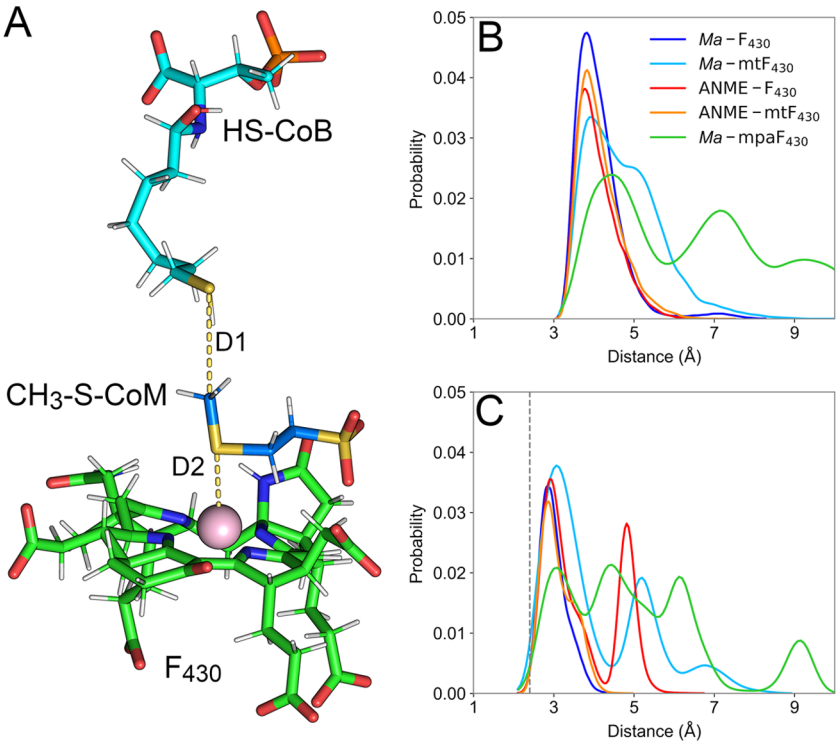

Figure 3. Overall cofactor and substrate coordination. (A) Prereaction scheme of MCR bound to F_{430}, CH_3-S-CoM, and HS-CoB. Key distances were designated as D1 and D2, representing the distance between the methyl group of CH_3-S-CoM and the thiol sulfur atom of HS-CoB and the distance between Ni(I) of F_{430} variants and the thioether sulfur atom of CH_3-S-CoM, respectively. (B) Distribution probability of distance D1 for each of the enzyme:cofactor complexes studied here. (C) Distribution probability of distance D2 for the same systems. The gray dashed line represents the crystallographic distance, for reference.

active site and thus did not include the active site water molecules in subsequent simulations. Further studies should be carried out to more confidently determine if the observed electron densities represent water molecules and, if so, what role they may have in the active sites. Alternatively, such electron densities could represent other apolar species with a similar number of electrons, such as trapped methane, as previously suggested.[28]

Active Site Structure and Dynamics. To explore the structural features adopted by MCRs from *M. acetivorans* compared to ANME-1, we evaluated the active site dynamics of the two enzymes in the presence of the canonical F_{430} compared to mtF_{430}. Recently, we have identified a modified F_{430} in *M. acetivorans* with a structure that we preliminarily assign as 17^2-mercaptopropanamide-F_{430} ($mpaF_{430}$, Figure 1C, see the Supporting Information). Thus, simulations were additionally performed with this extended mercaptopropanamide modification.

To evaluate the dynamics in all systems and their impact on the coordination among F_{430}, CH_3-S-CoM, and HS-CoB, we calculated two key distances related to their positioning in the active site (Figure 3). We defined D1 as the distance between the methyl carbon of CH_3-S-CoM and the sulfur atom of HS-CoB and D2 as the distance between the Ni(I) of F_{430} and the thioether sulfur of CH_3-S-CoM. Given the symmetry between active sites A and B, we pooled the data of both sites for each system and analyzed them together.

For all replicates of the *Ma*-F_{430} and ANME-mtF_{430} systems, D1 and D2 were consistent throughout the trajectories and coordination among cofactors was well maintained. The time series of D1 and D2 for all systems and replicates are shown in Figures S2 and S3. For ANME-mtF_{430}, D1 and D2 averaged at 4.2 ± 0.5 and 3.1 ± 0.4 Å, respectively. For *Ma*-F_{430}, D1 and D2 averaged at 4.1 ± 0.5 and 3.7 ± 0.9 Å, respectively. It is important to note that the reference crystal structures for both systems were obtained with HS-CoM present in the active site, which yields a smaller distance for D2 of 2.4 Å, likely due to a stronger interaction between nickel and a thiol/thiolate compared to a thioether.

The presence of Val419 in the α subunit of ANME-1 MCR creates a pocket that accommodates the F_{430} modification in the 17^2 position.[18] To test the impact of the methylthio group of mtF_{430} in maintaining the ANME-1 MCR active site structure, we simulated ANME-1 MCR bound to unmodified F_{430}. In our ANME-F_{430} simulations, some replicates maintained the canonical coordination between F_{430} and CH_3-S-CoM. D1 had an average of 4.1 ± 0.5 Å across all replicates, but D2 varied among replicate simulations and active sites. For the first replicate, D2 averaged 3.1 ± 0.4 Å in active site A and 3.2 ± 0.4 Å in active site B. For the second and third replicates, D2 increased in one of the active sites (average of 4.8 ± 0.5 Å) while maintaining an average of 3.0 ± 0.4 Å (Figure 4A) at the other active site. The increase in D2 corresponded to the diffusion of HS-CoB further into the active site, forcing a dihedral rotation in CH_3-S-CoM that disrupted the surrounding hydrophobic cage structure, consequently increasing the distance between CH_3-S-CoM and the F_{430} core (Figure 4B).

In *M. acetivorans* MCR, Gln420 occupies the same site as Val419 in ANME-1 MCR, which is expected to create a steric clash with F_{430} cofactors containing a modification at the 17^2 position. In our simulations of *Ma*-$mpaF_{430}$ and *Ma*-mtF_{430}

https://doi.org/10.1021/acs.biochem.4c00168
Biochemistry 2024, 63, 1783−1794

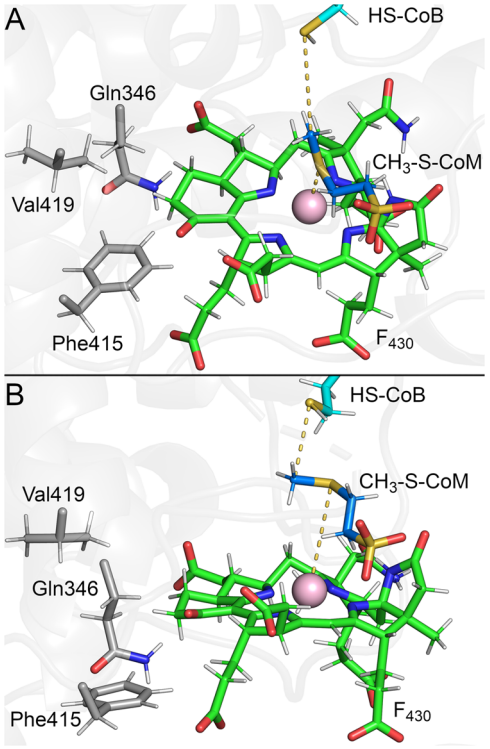

Figure 4. Cofactor coordination in ANME-F_{430}. (A) ANME-1 MCR bound to unmodified F_{430} (green), CH_3-S-CoM (blue), and HS-CoB (cyan). Key MCR residues are shown as sticks. Representative structure of canonical coordination among cofactors observed in our simulations. (B) Representative structure of the increased D2 between CH_3-S-CoM and F_{430}.

systems, the F_{430} modifications in the 17^2 position impacted the coordination between cofactors. In most replicates of *Ma*-$mpaF_{430}$, the large mercaptopropanamide group clashed with Gln420 and interacted with Phe416, which destabilized the coordination between CH_3−S-CoM and $mpaF_{430}$ (Figure 5A). In one replicate, however, the mercaptopropanamide group was able to displace Gln420 and accommodate itself between Phe416 and Gln345 (Figure 5B), thus maintaining the canonical coordination among the cofactors throughout the simulation. In another replicate in which the mercaptopropanamide group adopted an extended conformation, the canonical coordination between CH_3-S-CoM and $mpaF_{430}$ through the thioether sulfur−Ni(I) interaction was broken, and following a rearrangement, CH_3-S-CoM interacted with $mpaF_{430}$ via its sulfonate group for over 80 ns, resembling the pose in the reaction mechanism proposed by Patwardhan et al.[14] Such an alternative pose was observed in only one active site and in conjunction with a disruption of the hydrophobic cage surrounding the methylthio group of CH_3-S-CoM. This pose yielded D1 and D2 distances of 4.4 ± 0.7 and 5.8 ± 0.7 Å, respectively, while the average minimum distance between the sulfonate oxygen atoms and the Ni(I) of $mpaF_{430}$ was 1.8 ± 0.1 Å (Figure 5C).

For *Ma*-mtF_{430}, the methylthio group of mtF_{430} also suffered from steric clashes with Gln420, but to a lesser extent due to reorganization within the active site in some cases. In the replicates in which the mtF_{430} methylthio group was better accommodated in the active site, D1 and D2 averaged 3.4 ± 0.5 and 4.6 ± 0.8 Å, respectively, maintaining the canonical coordination among the cofactors. In these cases, Phe416 and Gln345 maintained their original interactions with mtF_{430}, while Gln420 repositioned to better accommodate the methylthio group (Figure 5D). In the replicates in which the coordination was lost, Gln345 shifted within the active site, leading to a change in the mtF_{430} 6-member ring puckering conformation that destabilized the coordination between CH_3-

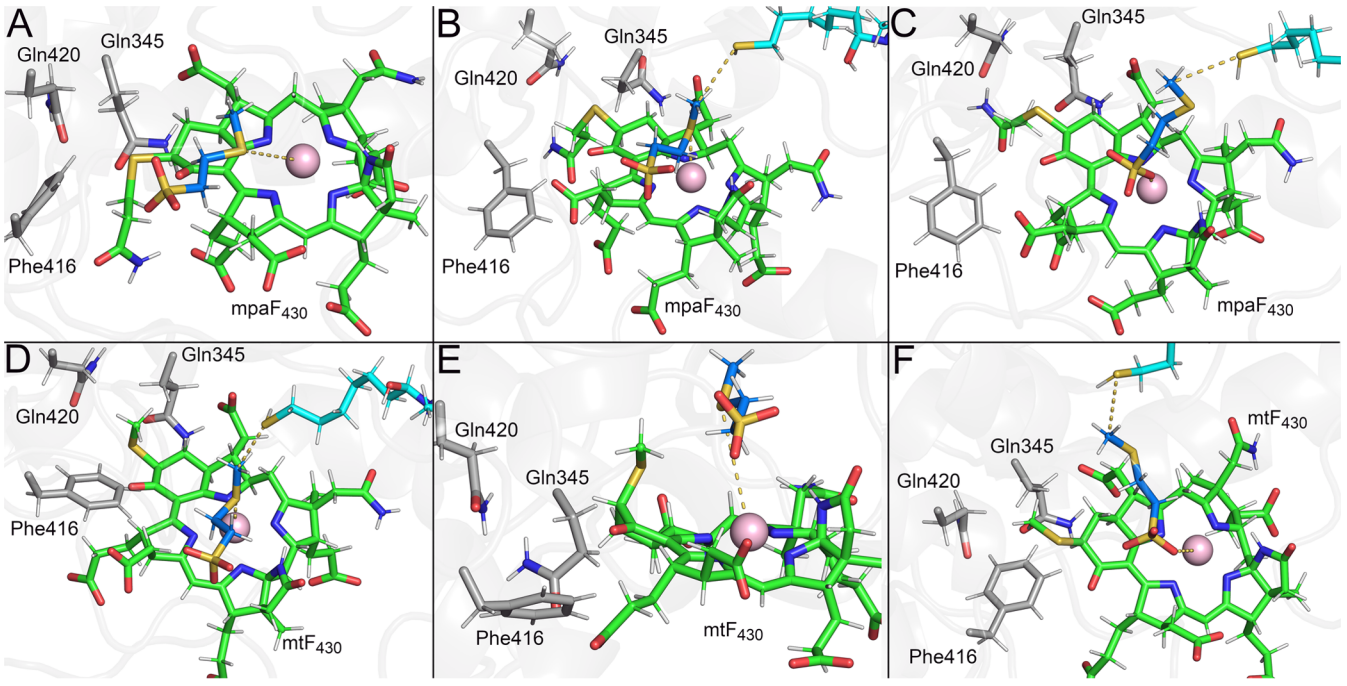

Figure 5. Cofactor coordination in *Ma*-$mpaF_{430}$ and *Ma*-mtF_{430}. (A−C) Representative structures of *M. acetivorans* MCR bound to $mpaF_{430}$ (green), CH_3-S-CoM (blue), and HS-CoB (cyan) sampled in our simulations. Key MCR residues are shown in gray sticks. (D−F) Representative structures of *M. acetivorans* MCR bound to mtF_{430} (green).

https://doi.org/10.1021/acs.biochem.4c00168
Biochemistry 2024, 63, 1783−1794

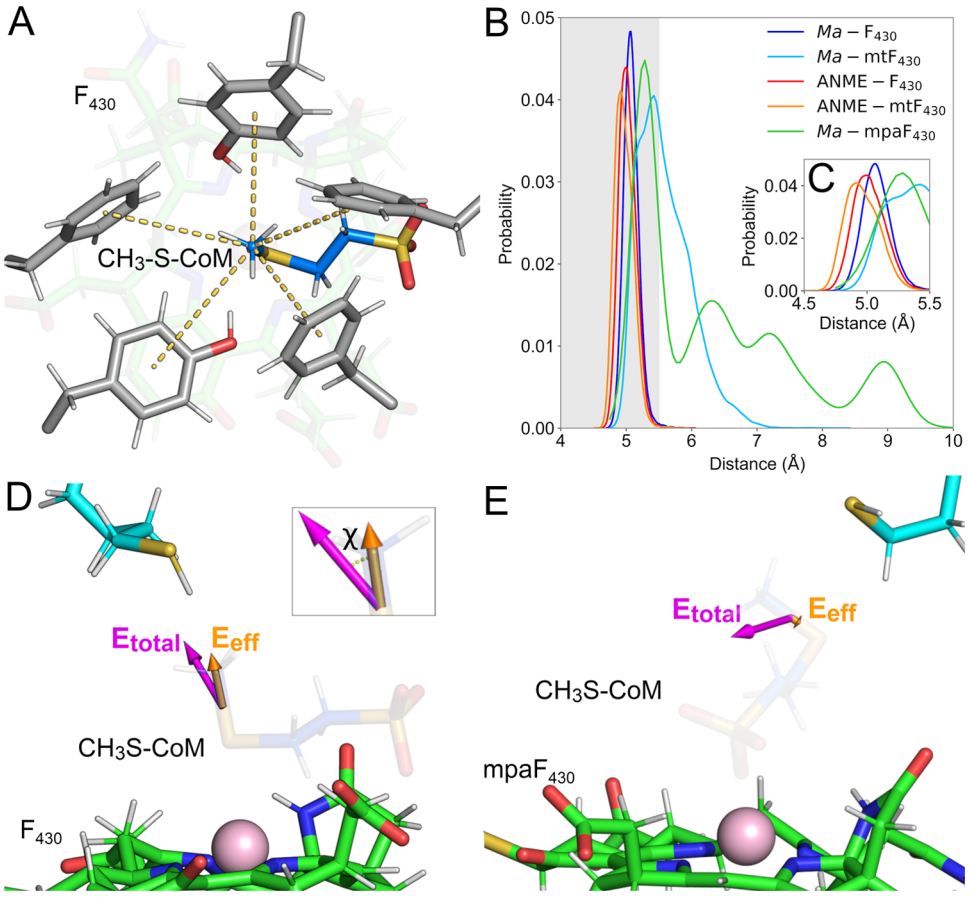

Figure 6. Overall organization of hydrophobic cage. (A) Prereaction scheme of MCR bound to F_{430}, CH_3-S-CoM, and HS-CoB. Conserved residues comprising the hydrophobic cage are shown in gray and their distances to the methyl group of CH_3-S-CoM are highlighted in yellow. (B) Probability distribution of $D3_{avg}$ composed of distances highlighted in panel (A) for each of the enzyme:cofactor complexes studied here. Gray areas represent commonly observed distances for hydrophobic interactions. (C) Highlight of the distributions between 4.5 and 5.5 Å. (D) Total and effective electric fields (magenta and orange, respectively) exerted by MCR, HS-CoB, and F_{430} acting at the S-CH_3 bond of CH_3-S-CoM. The inset depicts the angle χ measuring the alignment between $\vec{E}_{total}$ and E_{eff} field vectors. (E) Total and effective electric fields (magenta and orange, respectively) exerted by MCR, HS-CoB, and $mpaF_{430}$ acting at the S-CH_3 bond of CH_3-S-CoM in its alternative pose.

S-CoM and the mtF_{430} core due to a steric clash between the F_{430} methylthio group and CH_3-S-CoM (Figure 5E). Analogous to the alternative pose observed in *Ma*-$mpaF_{430}$ (Figure 5C), one replicate of our *Ma*-mtF_{430} simulations sampled a configuration in which the sulfonate group of CH_3-S-CoM was positioned near Ni(I) (Figure 5F), although a larger distance was observed (average minimum distance between Ni(I) and the sulfonate oxygens was 3.9 ± 0.2 Å), indicating that the sulfonate was not interacting directly with the Ni(I) of mtF_{430}. In that pose, D1 and D2 averaged 4.5 ± 0.6 and 6.8 ± 0.6 Å, respectively. For *Ma*-mtF_{430} and *Ma*-$mpaF_{430}$, in which steric clashes with Gln420 were disruptive to the coordination between the cofactors, the RMSD of mtF_{430} and $mpaF_{430}$ were consistently between 1 and 2 Å, suggesting some degree of conformational adaptation of these molecules that impacted the coordination between cofactors (Figure S4). For all other systems, the RMSD of F_{430} and mtF_{430} molecules were consistently below 1 Å, suggesting lesser deviation from the original crystallographic conformations.

The sulfonate-Ni(I) binding mode for CH_3-S-CoM was recently reported on the basis of detailed experimental work and density functional theory calculations.[14] Since we observed versions of this binding pose in some replicates of our MD simulations with *M. acetivorans* MCR in the presence of 17^2-modified F_{430} (Figure 5C,F), we wanted to further explore whether this CH_3-S-CoM binding pose was stable in conjunction with unmodified F_{430}. Thus, the system coordinates of the *Ma*-$mpaF_{430}$ replicate with the sulfonate-Ni(I) interaction (Figure 5C) were used as a starting point for new simulations in which the $mpaF_{430}$ was converted into the canonical F_{430}. It is important to note that only one active site (Site B) contains the alternate pose while the other maintains the thioether-Ni(I) interaction. We observed that the sulfonate-Ni(I) interaction was very strong in all of the replicates (Figure S5). However, the distance between the methyl group of CH_3-S-CoM and the sulfur of HS-CoB fluctuated more. In replicate 2, HS-CoB slid out of the active site, increasing the mentioned distance. In all replicates, the hydrophobic cage remained disrupted as observed for *Ma*-$mpaF_{430}$, yielding much more flexibility in the methylthio group of CH_3-S-CoM (Figure S6). Overall, these results support the feasibility of the alternate binding pose for CH_3-S-CoM but also indicate that the active site is more dynamic upon adoption of this configuration.

During our analyses of the different systems studied here, we identified key hydrophobic cage residues important for the overall active site structure and dynamics. As shown in Figure 2, the presence of conserved Phe and Tyr residues in the

https://doi.org/10.1021/acs.biochem.4c00168
Biochemistry 2024, 63, 1783−1794

hydrophobic cage surrounding the CH_3-S-CoM binding site suggests the importance of aromatic character within the active site microenvironment for the reaction being catalyzed. To better understand the organization of such structures throughout our simulations of each enzyme:cofactor system, we calculated the average of the distances between the aromatic residues comprising the cage and the methyl group of CH_3-S-CoM, from now on referred to as $D3_{avg}$ (Figure 6A,B). For *M. acetivorans* MCR, these residues were defined as Phe343, Tyr346, and Phe463 of subunit α, and Phe359 and Tyr365 of subunit β (Figure 2). In ANME-1 MCR, residues Phe344, Tyr347, and Phe462 of subunit α, and Phe357 and Tyr363 of subunit β were used.

For systems *Ma*-F_{430}, ANME-mtF_{430}, and ANME-F_{430}, $D3_{avg}$ values were 5.1 ± 0.1, 5.0 ± 0.1, and 5.0 ± 0.1 Å, respectively. As shown in Figure 6C, ANME-mtF_{430} and ANME-F_{430} sampled lower $D3_{avg}$ values slightly more often in comparison to *Ma*-F_{430}. Not surprisingly, these are the systems in which the canonical coordination among cofactors was better maintained throughout the simulations, suggesting that the hydrophobic cage also plays a structural role in maintaining the overall active site configuration. For systems *Ma*-mtF_{430} and *Ma*-mpaF_{430}, in which the canonical coordination among cofactors was less frequently observed, $D3_{avg}$ values were 5.6 ± 0.4 and 6 ± 1 Å, respectively, with broad distribution including longer distance values. These results emphasize the correlation between the loss of canonical coordination between cofactors and the cage structural organization, and stress the structural impact of the steric clash between F_{430} modifications and active site residues, especially Gln420 of subunit α.

MCR Electric Fields Driving Catalysis. The superior affinity of an enzyme to its reaction's transition state is derived from both conformational and electronic properties.[31,32] The role of intrinsic electric fields driving enzyme-mediated catalysis was proposed by Warshel in the 1970s[31,33,34] and gained traction more recently with the development of more robust computational models and experimental techniques to measure such effects.[32,35−37] Electric fields exerted by enzymes act at specific chemical bonds of the substrate, lowering the reaction activation barrier and stabilizing the transition state.

For the methane formation reaction catalyzed by MCR (Figure 1A), the working mechanism involves one-electron chemistry such that the thioether bond of CH_3-S-CoM is homolytically cleaved, forming a methyl radical and a Ni(II)-S-CoM intermediate. To understand how MCR organizes its active site electronic environment to drive methane synthesis, we calculated the total electric field ($\vec{E}_{total}$) acting at the center of thioether S-CH_3 bond of CH_3-S-CoM (Figure 6D) for each enzyme:cofactor system. From $\vec{E}_{total}$, we calculated the effective electric field ($\vec{E}_{eff}$), which is the vectorial projection of $\vec{E}_{total}$ onto the bond and represents the field that is effectively modulating the bond dipole. Finally, we also calculated an angle, χ, between the $\vec{E}_{total}$ and $\vec{E}_{eff}$ field vectors as a measure of their alignment (Figure 6D, inset). The value of χ allows us to determine how efficient the total electric field is in promoting the desired chemical reaction. To allow cross-comparison between different systems, we only considered the active sites and replicates in which the canonical coordination among the cofactors were reasonably maintained.

As represented in Figure 6D, $\vec{E}_{total}$ values of all systems were mainly positive, meaning they were oriented in the same direction as the bond dipole vector (S → CH_3). The good alignment between $\vec{E}_{total}$ and the bond implies that such a field is able to polarize the bond dipole even further and facilitate bond cleavage. As shown in Table 1, the average $\vec{E}_{total}$ values for *Ma*-F_{430}, *Ma*-mtF_{430}, and *Ma*-mpaF_{430} were 52 ± 13, 55 ± 13, and 54 ± 14 MV/cm, respectively. For ANME-mtF_{430} and ANME-F_{430}, the average $\vec{E}_{total}$ values were 67 ± 13 and 58 ± 12 MV/cm, respectively.

Table 1. MCR Intrinsic Electric Field Values Acting at the Thioether Bond of CH_3-S-CoM

system	average $\vec{E}_{total}$ (MV/cm)	average $\vec{E}_{eff}$ (MV/cm)	alignment angle χ (deg)
Ma-F_{430}	52 ± 13	39 ± 13	39 ± 16
Ma-mtF_{430}	55 ± 13	34 ± 15	42 ± 21
Ma-mpaF_{430}	54 ± 14	19 ± 12	69 ± 13
ANME-mtF_{430}	67 ± 13	56 ± 14	30 ± 16
ANME-F_{430}	58 ± 12	50 ± 13	28 ± 14

Except for ANME-mtF_{430}, the average $\vec{E}_{total}$ for all systems was close to ∼55 MV/cm, which can be considered weak in comparison to previous reports for other enzymes.[35,38] This property may be related to the homolytic bond cleavage as opposed to heterolytic bond cleavage. For $\vec{E}_{eff}$, ANME-mtF_{430} and ANME-F_{430} presented higher averages, specifically measuring 56 ± 14 and 50 ± 13 MV/cm, respectively, whereas *Ma*-F_{430}, *Ma*-mtF_{430}, and *Ma*-mpaF_{430} produced $\vec{E}_{eff}$ averages of 39 ± 13, 34 ± 15, and 19 ± 12 MV/cm, respectively.

The pronounced differences in $\vec{E}_{eff}$ of each system reflect the alignment between the total field and the bond. As shown in Table 1, the χ angle differed among systems, suggesting the active site conformation does impact $\vec{E}_{eff}$. The *Ma*-mpaF_{430} and *Ma*-mtF_{430} systems had the largest χ average angle across the systems, 69 ± 13 and 42 ± 21°, respectively, implying that these active site conformations and the hydrophobic cage organization are the most perturbed. In fact, even in maintaining the canonical cofactor coordination, *Ma*-mpaF_{430} had a $D3_{avg}$ of 5.9 ± 0.3 Å, highlighting the extent to which the active site structural organization impacts intrinsic electric fields in MCR. Interestingly, the lowest average χ angle values across the systems were observed for ANME-mtF_{430} and ANME-F_{430}, suggesting that the ANME-1 MCR active site optimizes the electric field acting on the thioether S-CH_3 bond of CH_3-S-CoM. A complete time series of $|\vec{E}_{eff}|$ values for all systems is shown in Figure S7.

These results are interesting since ANME-1 MCR catalyzes the reverse reaction (methane oxidation) *in vivo* but both of our systems using ANME-1 yielded stronger $\vec{E}_{eff}$ values in comparison to *M. acetivorans*, suggesting a better catalytic efficiency of the former in comparison to the later. However, given the complex electronic nature of the active site residues and cofactors involved in the reaction, a proper quantitative confirmation of the magnitudes observed in this work should be reassessed by models capturing electronic polarization effects.

To further decompose the contributions of different active site residues to $\vec{E}_{eff}$ in each system, we calculated the contribution of only the hydrophobic cage residues, finding that they may be responsible for up to half of the magnitude of $\vec{E}_{eff}$. As shown in Table 2, these residues contributed 12 ± 11, 20 ± 13, and 6 ± 10 MV/cm for systems *Ma*-F_{430}, *Ma*-mtF_{430}, and *Ma*-mpaF_{430}, respectively, while analogous hydrophobic cage residues of ANME-1 contributed 24 ± 13 and 21 ± 11

https://doi.org/10.1021/acs.biochem.4c00168
Biochemistry 2024, 63, 1783−1794

Table 2. Contribution of Hydrophobic Cage Residues to MCR Intrinsic Electric Field Values Acting at the Thioether Bond of CH_3-S-CoM

system	average $\vec{E}_{eff}$ (MV/cm)
Ma-F_{430}	13 ± 11
Ma-mtF_{430}	20 ± 13
Ma-mpaF_{430}	6 ± 10
ANME-mtF_{430}	24 ± 13
ANME-F_{430}	21 ± 11

MV/cm for systems ANME-mtF_{430} and ANME-F_{430}, respectively. These results correlate with the $D3_{avg}$ distances shown in Figure 6C, in which ANME-mtF_{430} and ANME-F_{430} sampled shorter distances more frequently than other systems. These results suggest the hydrophobic cage residues not only play a structural role in maintaining the canonical coordination among cofactors but also play an electronic role in contributing a major part of the electric field driving methane formation.

Moreover, we evaluated the same electric field organized by MCR but now considering the alternative pose observed for *Ma*-mpaF_{430} and *Ma*-F_{430}, and similar to the alternative binding scheme leading to the long-range electron transfer mechanism proposed by Patwardhan et al.[14] (Figure 6E). Throughout the trajectories, the structure of the hydrophobic cage residues surrounding CH_3-S-CoM was very poorly maintained in both systems, with a $D3_{avg}$ of 6.5 ± 0.6 and 6.3 ± 0.6 Å for *Ma*-mpaF_{430} and *Ma*-F_{430} respectively, yielding an average $\vec{E}_{total}$ of 35 ± 8 and 31 ± 8 MV/cm for *Ma*-mpaF_{430} and *Ma*-F_{430}, respectively. At the same time, the methyl group of CH_3-S-CoM presented an increased degree of flexibility in both systems (Figure S7), often rotating about the thioether bonds while still maintaining the interaction between CH_3-S-CoM and mpaF_{430} or F_{430} molecules through its sulfonate group (Figure S7). Due to its high mobility, $\vec{E}_{total}$ was generally poorly aligned with the thioether S-CH_3 bond (average χ values of 64 ± 20 and 53 ± 32° for *Ma*-mpaF_{430} and *Ma*-F_{430}, respectively), often sampling electric fields nearly perpendicular to the bond, resulting in a very weak $\vec{E}_{eff}$ (average of 16 ± 12 and 17 ± 14 MV/cm for *Ma*-mpaF_{430} and *Ma*-F_{430}, respectively). Given the weak $\vec{E}_{eff}$ acting on the thioether bond in the frames sampling the alternative pose of CH_3-S-CoM within the active sites, it is unlikely that such a field would be able to increase the CH_3−S bond dipole and facilitate bond cleavage, as we observe for the canonical binding pose. However, since our analyses reported here show that the 17^2 F_{430} modifications result in large perturbations to the *M. acetivorans* MCR active site, other aspects of the reorganization may be responsible for the impact on the measured electric fields. Additionally, we recognize that these fields should be recalculated with models with more robust electronic description to account for the intricate electronic properties of the active site microenvironment.

CONCLUSIONS

Through our MD simulations, we provided key insights into the active site dynamics of MCRs from *M. acetivorans* and ANME-1 when bound to modified F_{430} cofactors and substrates for the methane formation reaction. First, we investigated the presence of electron densities inside the active site commonly modeled as water molecules in X-ray structures. Our simulations suggest that the presence of a water molecule inside a hydrophobic cage composed of aromatic residues surrounding CH_3-S-CoM is unlikely to be favorable, given the chemical nature of the active site and the rapid expulsion of the water molecules in both active sites all our simulations. Our observations indicate that future studies are still necessary to determine the chemical nature of these observed electron densities.

Our simulations enabled us to characterize the dynamics of enzyme:cofactor complexes with F_{430} variants containing modifications in the 17^2 position and their relationship with active site dynamics. In all replicates of *Ma*-F_{430} and ANME-mtF_{430}, we were able to reasonably capture the active site structure and canonical cofactor coordination. Moreover, we demonstrated the impact of the steric clash between Gln420 of *M. acetivorans* MCR subunit α and the 17^2 methylthio and 3-mercaptopropanamide-F_{430} modifications on the active site structure. The presence of bulkier groups perturbed the active site interaction network and impacted the structural organization of the hydrophobic cage residues surrounding CH_3-S-CoM, in turn leading to the loss of the canonical coordination among cofactors representing the precatalytic state. However, we did observe some evidence of active site reorganization that better maintained the canonical configuration and suggests that modifications could potentially be accommodated. Interestingly, we also observed an alternate binding pose in some replicates of *M. acetivorans* MCR with mpaF_{430} and mtF_{430} in which CH_3-S-CoM interacts with Ni(I) through its sulfonate group instead of the thioether sulfur. Thus, F_{430} modifications could play a role in optimizing the positions of the substrates and/or products to facilitate catalysis or product release. In ANME-1, Val419 of subunit α occupies the analogous position as Gln420 of *M. acetivorans*, creating a suitable pocket to accommodate the 17^2 methylthio group of mtF_{430}. In simulations of ANME-F_{430}, the absence of the methylthio group also impacted the active site structure and led to some loss of the canonical cofactor coordination, although to a lesser extent when compared to systems *Ma*-mtF_{430} and *Ma*-mpaF_{430}.

Finally, we characterized the intrinsic electric fields organized by MCR in its active sites to drive the methane formation reaction. We showed that MCR exerts an electric field aligned with the thioether bond of CH_3-S-CoM, which polarizes the bond dipole and facilitates homolytic bond cleavage and the formation of the methyl radical. Such an electric field is in line with the prevailing hypothesis for the mechanism through which this reaction proceeds. Moreover, we also demonstrated how these fields are sensitive to the hydrophobic cage structural organization. In the replicates in which the structure was perturbed, the total electric field was weaker and misaligned with the bond. Yet, due to the complex electronic nature of the active site molecular components, the electric fields studied here should be revisited by future efforts employing electronically polarizable models to quantitatively capture intricate electronic properties of MCR active sites.

Overall, our results contribute to a better understanding of MCR active site dynamics and the impact of F_{430} modifications, as well as how the enzyme organizes intrinsic electric fields to drive catalysis and the role of the active site structure in the maintenance of such fields.

MATERIALS/EXPERIMENTAL DETAILS

Parametrization of Cofactors. Parameters for methyl-coenzyme M (CH_3-S-CoM) and coenzyme B (HS-CoB) were obtained from the CHARMM General Force Field (CGenFF) version 4.6.[39] Initial parameters for F_{430} with no Ni(I) ion were

https://doi.org/10.1021/acs.biochem.4c00168
Biochemistry 2024, 63, 1783−1794

obtained in a similar manner. Lennard-Jones (LJ) parameters for Ni(I) were fit to water interaction energies from quantum mechanical (QM) calculations. A rigid optimization of Ni(I) with a water molecule (held in TIP3P geometry) was performed to identify the distance of optimal interaction between the ion and water. This optimization was performed with a B971/cc-pVQZ model chemistry, as suggested for transition elements.[40] The interaction energy between these species was then calculated using the same model chemistry, with counterpoise correction for basis set superposition error.[41,42] All QM calculations were performed in Gaussian09.[43] The final LJ parameters for Ni(I) were $R_{min}/2$ = 0.7811 Å and ε = −0.02 kcal/mol.

To enforce the proper coordination geometry of Ni(I) in the macrocyclic ring, harmonic bond terms were added between Ni(I) and the pyrrole nitrogen atoms with a force constant of 500 kcal/mol·Å^2 and b_0 of 2.06 Å. Force constants were set to zero for angles and proper dihedral terms involving Ni(I) and the macrocyclic ring, following the CHARMM force field convention to omit explicit contribution to the forces arising from these interactions when involving metals. Improper dihedrals based on the heme residue were added to enforce planarity of the Ni(I) ion within the macrocyclic ring. Afterward, we refined macrocyclic internal bonds and angles to reproduce the ring puckering and overall macrocyclic conformation from crystallographic data. The final parameters for F_{430} served as the basis to derive mtF_{430}. Additional parameters for methylthio and mercaptopropanamide group substitutions were obtained through CGenFF in a similar manner and later merged with the F_{430} parameters to create the mtF_{430} and mercaptopropanamide-F_{430} residues ($mpaF_{430}$). Topology parameters for all cofactors described in this work are available in the Supporting Information.

Molecular Dynamics System Setup. To understand the structural relationship between ANME-1 and *M. acetivorans* MCR complexes when bound to different F_{430} cofactors, we built four simulation systems (Table 3). To build system *Ma*-F_{430}, the atomic coordinates of *M. acetivorans* MCR bound to F_{430} reported by Nayak et al.[27] were used. For system ANME-mtF_{430}, the coordinates for ANME-1 MCR complex bound to mtF_{430} were obtained from PDB 3SQG.[18] To build system ANME-F_{430}, we simply aligned systems *Ma*-F_{430} and ANME-mtF_{430} and transposed the coordinates of each F_{430} molecule to their corresponding active sites. The preparation of the *Ma*-mtF_{430} and *Ma*-$mpaF_{430}$ systems are described below. Protein topologies were generated using CHARMM36m force field,[44] and specific parameters for nonstandard amino acids in the structure, namely, N^1-methylated histidine (MHS), 5-methylarginine (AGM), thioglycinethioglycin (GL3), didehydroaspartate (DYA), S-methylcysteine (SMC), and 7-hydroxytryptophan (0AF), were obtained from the work of Croitoru et al.[45] The N- and C-termini of each MCR protein chain were capped with a protonated amine and a deprotonated carboxylate group, respectively. Protonation states of histidine, aspartate, and glutamate residues were assigned by using the PlayMolecule web server based on pK_a calculations[46] and visually checked to ensure an optimized hydrogen-bonding network (Tables S1 and S2). Crystallographic waters were retained for all systems except for two water molecules modeled between CoM and CoB in both active sites in the crystal structure reported by Nayak et al., for the reasons described below. Methyl groups of CH_3-S-CoM in both active sites were rebuilt using CHARMM internal coordinate builder.[47] Each enzyme:cofactor complex was solvated in a cubic box of CHARMM-modified TIP3P water[48−50] and ∼150 mM KCl, including necessary counterions.

Table 3. Composition of Each System in This Work

system ID	organism	F_{430} cofactor	ions (K^+/Cl^-)	no. of waters
Ma-F_{430}	*M. acetivorans*	F_{430}	304/242	258 030
Ma-mtF_{430}	*M. acetivorans*	mtF_{430}	304/242	258 054
Ma-$mpaF_{430}$	*M. acetivorans*	$mpaF_{430}$	304/242	258 099
ANME-F_{430}	ANME-1	F_{430}	291/235	249 030
ANME-mtF_{430}	ANME-1	mtF_{430}	291/235	249 081

The CHARMM package[47] was used to perform energy minimizations using the steepest descent algorithm for 100 steps, followed by 500 steps of adopted-basis Newton−Raphson minimization to relax steric clashes. Equilibration of solvent and bulk ions was performed via three independent replicates for 1 ns using OpenMM[51] version 7.7 with a position restraint force constant of 800 kJ/(mol·nm^2) on all heavy atoms, including those of the cofactors. A 2 fs integration step was used with a Langevin integrator and a temperature of 310 K, while a Monte Carlo barostat algorithm was applied to maintain the pressure at 1 bar. Short-range van der Waals forces were switched smoothly to zero from 10 to 12 Å and electrostatic interactions were calculated via the Particle Mesh Ewald method[52,53] with a real-space cutoff of 12 Å. The equilibrated system coordinates of all 3 replicates were submitted to unrestrained production runs of 100 ns each, while saving coordinates every 10 ps.

As mentioned before, the presence of Val419 in the α subunits of ANME-1 MCR accommodates the methylthio group of mtF_{430},[1818] whereas methanogen MCRs possess a glutamine in the same position that could result in steric clashes with the modifications at the 17^2 position of F_{430}, i.e., the methylthio group in mtF_{430} or the mercaptopropanamide group in $mpaF_{430}$. To study possible active site rearrangements necessary to properly fit 17^2-modified F_{430}'s into the *M. acetivorans* MCR binding site, we built system *Ma*-mtF_{430} and *Ma*-$mpaF_{430}$ by applying an alchemical transformation protocol: electrostatic and Lennard-Jones potentials of the modified F_{430} cofactors were switched from 0 (no interaction) to 1 (full interaction) in a stepwise manner through a λ scaling factor applied to the Hamiltonian.[54,55] Lennard-Jones potentials were switched on first (λ = 0.00, 0.05, 0.10,0.15, 0.20, 0.30, ..., 0.70, 0.75, 0.80, 0.85, 0.90, 0.95, 1.00) and electrostatic interactions were switched on afterward (λ = 0.00, 0.10, 0.20, ..., 0.80, 0.90, 1.00). Such an approach allows for a gentle adjustment of the protein binding site residues. We built the system using CHARMM as described above. Before energy minimization, the system's coordinates were used to rebuild their topologies in GROMACS using the *pdb*2gmx utility. The cofactor force field parameters were converted to GROMACS format using the *cgenff_charmm2gmx.py* script available at https://github.com/Lemkul-Lab/cgenff_charmm2gmx. The alchemical transformation protocol in each λ window consisted of (a) energy minimization using steepest descent algorithm for 1000 steps, followed by another energy minimization using the conjugate gradient algorithm for 1000 steps; (b) an equilibration under an NPT ensemble using position restraints on all heavy atoms [force constant of 800 kJ/(mol·nm^2)] for 100 ps using the nonbonded interaction parameters described

https://doi.org/10.1021/acs.biochem.4c00168
Biochemistry 2024, 63, 1783−1794

above and (c) an unrestrained production run for 1 ns. Soft-core α and σ parameters were set to 0.5 and 0.3, respectively. $\partial H/\partial\lambda$ and ΔH values were written every 0.02 ps. Throughout the protocol, we applied flat-bottom restraints as shown in Figure S8 to preserve the overall orientation of the F_{430} cofactors relative to their respective binding sites. The initial restraining force constant of 200 kJ/(mol·nm^2) was decreased linearly as the λ value increased such that the force constant was zero when $\lambda = 1$. The last frame of the production run in each λ window was used as input for the minimization step of the next λ window. At the completion of the alchemical transformation, the last frame of the $\lambda = 1$ production run was used to initiate three independent replicas following the 1 ns equilibration and 100 ns production protocols used for the other systems.

Electric Field Calculations. To understand the role of electrostatic forces on methane formation by MCR, we used TUPÃ[S6] to calculate the electric fields organized by the different MCR complexes acting on the methyl-sulfur bond of CH_3-S-CoM to facilitate its cleavage. We used the BOND mode and defined the bond vector as S → CH_3 such that any field vector aligned with the bond vector results in positive values. All protein, F_{430}, and HS-CoB atoms were included in the environment set (i.e., the atoms exerting the electric field) while the self-contribution of atoms in CH_3-S-CoM was ignored. The complete configuration parameters used in the calculation can be found in the Supporting Information.

■ ASSOCIATED CONTENT

Supporting Information

The Supporting Information is available free of charge at https://pubs.acs.org/doi/10.1021/acs.biochem.4c00168.

Additional methodological details for the characterization of mpaF_{430} and the flat-bottom restraint used during alchemical transformations, flat-bottom restraint scheme, analysis of water molecules exiting the active site, alternative poses of CH_3-S-CoM, time series of distances D1 and D2 and of F_{430} RMSD values for all replicates of each system, time series of the electric fields acting along the S-CH_3 bond, mass spectra and UV−vis spectrum of mpaF_{430}, protonation of titratable residues in each MCR, and the topologies and associated force field parameters for the F_{430} cofactors, CH_3-S-CoM, and HS-CoB. (PDF)

Movie S1: Dynamics of water initially occupying the MCR active site near the F_{430} cofactor. (MP4)

Accession Codes

M. acetivorans: McrA—WP_011024419.1, McrB—WP_011024423.1, McrG—WP_011024420.1; *M. maripaludis*: McrA—CAF31115.1, McrB—CAF31111.1, McrG—CAF31114.1; *M. marburgensis*: McrA—P11558.3, McrB—P11560.3, McrG—P11562.3; ANME-1: McrA—CBH39484.1, McrB—CBH39482.1, McrG—CBH39483.1; ANME-2d: McrA—SNQ61551.1, McrB—SNQ61548.1, McrG—SNQ61550.1.

■ AUTHOR INFORMATION

Corresponding Authors

Kylie D. Allen − *Department of Biochemistry, Virginia Tech, Blacksburg, Virginia 24061, United States;* orcid.org/0000-0002-6860-659X; Email: kdallen@vt.edu

Justin A. Lemkul − *Department of Biochemistry, Virginia Tech, Blacksburg, Virginia 24061, United States;* orcid.org/0000-0001-6661-8653; Email: jalemkul@vt.edu

Author

Marcelo D. Polêto − *Department of Biochemistry, Virginia Tech, Blacksburg, Virginia 24061, United States;* orcid.org/0000-0001-9210-690X

Complete contact information is available at: https://pubs.acs.org/10.1021/acs.biochem.4c00168

Notes

The authors declare no competing financial interest.

■ ACKNOWLEDGMENTS

The authors thank Kaleb Boswinkle and Aleksei Gendron for their work on identifying the proposed mpaF_{430} in *M. acetivorans*. They also thank Satish Nair and William W. Metcalf for providing the coordinates of *M. acetivorans* MCR, and Virginia Tech Advanced Research Computing for computing time and resources. This work was supported by the US Department of Energy (DOE), Office of Science, Basic Energy Sciences (BES) (Grant DE-SC0022338).

■ REFERENCES

(1) Lyu, Z.; Shao, N.; Akinyemi, T.; Whitman, W. B. Methanogenesis. *Curr. Biol.* **2018**, *28* (13), R727−R732.

(2) Moissl-Eichinger, C.; Pausan, M.; Taffner, J.; Berg, G.; Bang, C.; Schmitz, R. A. Archaea Are Interactive Components of Complex Microbiomes. *Trends Microbiol.* **2018**, *26* (1), 70−85.

(3) Borrel, G.; Brugère, J.-F.; Gribaldo, S.; Schmitz, R. A.; Moissl-Eichinger, C. The Host-Associated Archaeome. *Nat. Rev. Microbiol.* **2020**, *18* (11), 622−636.

(4) Conrad, R. The Global Methane Cycle: Recent Advances in Understanding the Microbial Processes Involved. *Environ. Microbiol. Rep.* **2009**, *1* (5), 285−292.

(5) Kirschke, S.; Bousquet, P.; Ciais, P.; Saunois, M.; Canadell, J. G.; Dlugokencky, E. J.; Bergamaschi, P.; Bergmann, D.; Blake, D. R.; Bruhwiler, L.; Cameron-Smith, P.; Castaldi, S.; Chevallier, F.; Feng, L.; Fraser, A.; Heimann, M.; Hodson, E. L.; Houweling, S.; Josse, B.; Fraser, P. J.; Krummel, P. B.; Lamarque, J.-F.; Langenfelds, R. L.; Le Quéré, C.; Naik, V.; O'Doherty, S.; Palmer, P. I.; Pison, I.; Plummer, D.; Poulter, B.; Prinn, R. G.; Rigby, M.; Ringeval, B.; Santini, M.; Schmidt, M.; Shindell, D. T.; Simpson, I. J.; Spahni, R.; Steele, L. P.; Strode, S. A.; Sudo, K.; Szopa, S.; van der Werf, G. R.; Voulgarakis, A.; van Weele, M.; Weiss, R. F.; Williams, J. E.; Zeng, G. Three Decades of Global Methane Sources and Sinks. *Nat. Geosci.* **2013**, *6* (10), 813−823.

(6) Jackson, R. B.; Saunois, M.; Bousquet, P.; Canadell, J. G.; Poulter, B.; Stavert, A. R.; Bergamaschi, P.; Niwa, Y.; Segers, A.; Tsuruta, A. Increasing Anthropogenic Methane Emissions Arise Equally from Agricultural and Fossil Fuel Sources. *Environ. Res. Lett.* **2020**, *15* (7), No. 071002.

(7) Thauer, R. K. Methyl (Alkyl)-Coenzyme M Reductases: Nickel F-430-Containing Enzymes Involved in Anaerobic Methane Formation and in Anaerobic Oxidation of Methane or of Short Chain Alkanes. *Biochemistry* **2019**, *58* (52), 5198−5220.

(8) Ermler, U.; Grabarse, W.; Shima, S.; Goubeaud, M.; Thauer, R. K. Crystal Structure of Methyl-Coenzyme M Reductase: The Key Enzyme of Biological Methane Formation. *Science* **1997**, *278* (5342), 1457−1462.

(9) Wongnate, T.; Sliwa, D.; Ginovska, B.; Smith, D.; Wolf, M. W.; Lehnert, N.; Raugei, S.; Ragsdale, S. W. The Radical Mechanism of Biological Methane Synthesis by Methyl-Coenzyme M Reductase. *Science* **2016**, *352* (6288), 953−958.

(10) Pelmenschikov, V.; Blomberg, M. R. A.; Siegbahn, P. E. M.; Crabtree, R. H. A Mechanism from Quantum Chemical Studies for Methane Formation in Methanogenesis. *J. Am. Chem. Soc.* **2002**, *124* (15), 4039−4049.
(11) Pelmenschikov, V.; Siegbahn, P. E. M. Catalysis by Methyl-Coenzyme M Reductase: A Theoretical Study for Heterodisulfide Product Formation. *J. Biol. Inorg. Chem.* **2003**, *8* (6), 653−662.
(12) Chen, S.-L.; Blomberg, M. R. A.; Siegbahn, P. E. M. An Investigation of Possible Competing Mechanisms for Ni-Containing Methyl−Coenzyme M Reductase. *Phys. Chem. Chem. Phys.* **2014**, *16* (27), 14029−14035.
(13) Chen, S.-L.; Blomberg, M. R. A.; Siegbahn, P. E. M. How Is Methane Formed and Oxidized Reversibly When Catalyzed by Ni-Containing Methyl-Coenzyme M Reductase? *Chem. − Eur. J.* **2012**, *18* (20), 6309−6315.
(14) Patwardhan, A.; Sarangi, R.; Ginovska, B.; Raugei, S.; Ragsdale, S. W. Nickel−Sulfonate Mode of Substrate Binding for Forward and Reverse Reactions of Methyl-SCoM Reductase Suggest a Radical Mechanism Involving Long-Range Electron Transfer. *J. Am. Chem. Soc.* **2021**, *143* (14), 5481−5496.
(15) Scheller, S.; Ermler, U.; Shima, S. Catabolic Pathways and Enzymes Involved in Anaerobic Methane Oxidation. In *Anaerobic Utilization of Hydrocarbons, Oils, and Lipids*; Boll, M., Ed.; Springer International Publishing: Cham, 2017; pp 1−29.
(16) Bhattarai, S.; Cassarini, C.; Lens, P. N. L. Physiology and Distribution of Archaeal Methanotrophs That Couple Anaerobic Oxidation of Methane with Sulfate Reduction. *Microbiol. Mol. Biol. Rev.* **2019**, *83* (3), No. e00074-18, DOI: 10.1128/mmbr.00074-18.
(17) Mayr, S.; Latkoczy, C.; Krüger, M.; Günther, D.; Shima, S.; Thauer, R. K.; Widdel, F.; Jaun, B. Structure of an F430 Variant from Archaea Associated with Anaerobic Oxidation of Methane. *J. Am. Chem. Soc.* **2008**, *130* (32), 10758−10767.
(18) Shima, S.; Krueger, M.; Weinert, T.; Demmer, U.; Kahnt, J.; Thauer, R. K.; Ermler, U. Structure of a Methyl-Coenzyme M Reductase from Black Sea Mats That Oxidize Methane Anaerobically. *Nature* **2012**, *481* (7379), 98−101.
(19) Allen, K. D.; Wegener, G.; White, R. H. Discovery of Multiple Modified F430 Coenzymes in Methanogens and Anaerobic Methanotrophic Archaea Suggests Possible New Roles for F430 in Nature. *Appl. Environ. Microbiol.* **2014**, *80* (20), 6403−6412.
(20) Hahn, C. J.; Lemaire, O. N.; Kahnt, J.; Engilberge, S.; Wegener, G.; Wagner, T. Crystal Structure of a Key Enzyme for Anaerobic Ethane Activation. *Science* **2021**, *373* (6550), 118−121.
(21) Bharadwaz, P.; Maldonado-Domínguez, M.; Chalupský, J.; Srnec, M. Reactivity Factors in Catalytic Methanogenesis and Their Tuning upon Coenzyme F430 Biosynthesis. *J. Am. Chem. Soc.* **2023**, *145* (16), 9039−9051.
(22) Wagner, T.; Wegner, C.-E.; Kahnt, J.; Ermler, U.; Shima, S. Phylogenetic and Structural Comparisons of the Three Types of Methyl Coenzyme M Reductase from Methanococcales and Methanobacteriales. *J. Bacteriol.* **2017**, *199* (16), No. e00197-17, DOI: 10.1128/jb.00197-17.
(23) Grabarse, W.; Mahlert, F.; Shima, S.; Thauer, R. K.; Ermler, U. Comparison of Three Methyl-Coenzyme M Reductases from Phylogenetically Distant Organisms: Unusual Amino Acid Modification, Conservation and adaptation. *J. Mol. Biol.* **2000**, *303* (2), 329−344.
(24) Cedervall, P. E.; Dey, M.; Li, X.; Sarangi, R.; Hedman, B.; Ragsdale, S. W.; Wilmot, C. M. Structural Analysis of a Ni-Methyl Species in Methyl-Coenzyme M Reductase from *Methanothermobacter marburgensis*. *J. Am. Chem. Soc.* **2011**, *133* (15), 5626−5628.
(25) Cedervall, P. E.; Dey, M.; Pearson, A. R.; Ragsdale, S. W.; Wilmot, C. M. Structural Insight into Methyl-Coenzyme M Reductase Chemistry Using Coenzyme B Analogues. *Biochemistry* **2010**, *49* (35), 7683−7693.
(26) Wagner, T.; Kahnt, J.; Ermler, U.; Shima, S. Didehydroaspartate Modification in Methyl-Coenzyme M Reductase Catalyzing Methane Formation. *Angew. Chem., Int. Ed.* **2016**, *55* (36), 10630−10633.
(27) Nayak, D. D.; Liu, A.; Agrawal, N.; Rodriguez-Carerro, R.; Dong, S.-H.; Mitchell, D. A.; Nair, S. K.; Metcalf, W. W. Functional Interactions between Posttranslationally Modified Amino Acids of Methyl-Coenzyme M Reductase in *Methanosarcina acetivorans*. *PLoS Biol.* **2020**, *18* (2), No. e3000507.
(28) Grabarse, W.; Mahlert, F.; Duin, E. C.; Goubeaud, M.; Shima, S.; Thauer, R. K.; Lamzin, V.; Ermler, U. On the Mechanism of Biological Methane Formation: Structural Evidence for Conformational Changes in Methyl-Coenzyme M Reductase upon Substrate Binding. *J. Mol. Biol.* **2001**, *309* (1), 315−330.
(29) Madeira, F.; Pearce, M.; Tivey, A. R. N.; Basutkar, P.; Lee, J.; Edbali, O.; Madhusoodanan, N.; Kolesnikov, A.; Lopez, R. Search and Sequence Analysis Tools Services from EMBL-EBI in 2022. *Nucleic Acids Res.* **2022**, *50* (W1), W276−W279.
(30) Robert, X.; Gouet, P. Deciphering Key Features in Protein Structures with the New ENDscript Server. *Nucleic Acids Res.* **2014**, *42* (W1), W320−W324.
(31) Warshel, A.; Sharma, P. K.; Kato, M.; Xiang, Y.; Liu, H.; Olsson, M. H. M. Electrostatic Basis for Enzyme Catalysis. *Chem. Rev.* **2006**, *106* (8), 3210−3235.
(32) Fried, S. D.; Boxer, S. G. Electric Fields and Enzyme Catalysis. *Annu. Rev. Biochem.* **2017**, *86*, 387−415.
(33) Warshel, A.; Levitt, M. Theoretical Studies of Enzymic Reactions: Dielectric, Electrostatic and Steric Stabilization of the Carbonium Ion in the Reaction of Lysozyme. *J. Mol. Biol.* **1976**, *103* (2), 227−249.
(34) Warshel, A. Electrostatic Origin of the Catalytic Power of Enzymes and the Role of Preorganized Active Sites. *J. Biol. Chem.* **1998**, *273* (42), 27035−27038.
(35) Fried, S. D.; Bagchi, S.; Boxer, S. G. Extreme Electric Fields Power Catalysis in the Active Site of Ketosteroid Isomerase. *Science* **2014**, *346* (6216), 1510−1514.
(36) Bradshaw, R. T.; Dziedzic, J.; Skylaris, C. K.; Essex, J. W. The Role of Electrostatics in Enzymes: Do Biomolecular Force Fields Reflect Protein Electric Fields? *J. Chem. Inf. Model.* **2020**, *60* (6), 3131−3144.
(37) Che, F.; Gray, J. T.; Ha, S.; Kruse, N.; Scott, S. L.; McEwen, J. S. Elucidating the Roles of Electric Fields in Catalysis: A Perspective. *ACS Catal.* **2018**, *8* (6), 5153−5174.
(38) Vaissier, V.; Sharma, S. C.; Schaettle, K.; Zhang, T.; Head-Gordon, T. Computational Optimization of Electric Fields for Improving Catalysis of a Designed Kemp Eliminase. *ACS Catal.* **2018**, *8* (1), 219−227.
(39) Vanommeslaeghe, K.; Hatcher, E.; Acharya, C.; Kundu, S.; Zhong, S.; Shim, J.; Darian, E.; Guvench, O.; Lopes, P.; Vorobyov, I.; Mackerell, A. D., Jr. CHARMM General Force Field: A Force Field for Drug-like Molecules Compatible with the CHARMM All-Atom Additive Biological Force Fields. *J. Comput. Chem.* **2010**, *31* (4), 671−690.
(40) Tekarli, S. M.; Drummond, M. L.; Williams, T. G.; Cundari, T. R.; Wilson, A. K. Performance of Density Functional Theory for 3d Transition Metal-Containing Complexes: Utilization of the Correlation Consistent Basis Sets. *J. Phys. Chem. A* **2009**, *113* (30), 8607−8614.
(41) Boys, S. F.; Bernardi, F. The Calculation of Small Molecular Interactions by the Differences of Separate Total Energies. Some Procedures with Reduced Errors. *Mol. Phys.* **1970**, *19* (4), 553−566.
(42) Ransil, B. J. Studies in Molecular Structure. IV. Potential Curve for the Interaction of Two Helium Atoms in Single-Configuration LCAO MO SCF Approximation. *J. Chem. Phys.* **1961**, *34* (6), 2109−2118.
(43) Frisch, M. J.; Trucks, G. W.; Schlegel, H. B.; Scuseria, G. E.; Robb, M. A.; Cheeseman, J. R.; Scalmani, G.; Barone, V.; Mennucci, B.; Petersson, G. A.; Nakatsuji, H.; Caricato, M.; Li, X.; Hratchian, H. P.; Izmaylov, A. F.; Bloino, J.; Zheng, G.; Sonnenberg, J. L.; Hada, M.; Ehara, M.; Toyota, K.; Fukuda, R.; Hasegawa, J.; Ishida, M.; Nakajima, T.; Honda, Y.; Kitao, O.; Nakai, H.; Vreven, T.; Montgomery, J. A., Jr.; Peralta, J. E.; Ogliaro, F.; Bearpark, M.; Heyd, J. J.; Brothers, E.; Kudin, K. N.; Staroverov, V. N.; Kobayashi,

https://doi.org/10.1021/acs.biochem.4c00168
Biochemistry 2024, 63, 1783−1794

R.; Normand, J.; Raghavachari, K.; Rendell, A.; Burant, J. C.; Iyengar, S. S.; Tomasi, J.; Cossi, M.; Rega, N.; Millam, J. M.; Klene, M.; Knox, J. E.; Cross, J. B.; Bakken, V.; Adamo, C.; Jaramillo, J.; Gomperts, R.; Stratmann, R. E.; Yazyev, O.; Austin, A. J.; Cammi, R.; Pomelli, C.; Ochterski, J. W.; Martin, R. L.; Morokuma, K.; Zakrzewski, V. G.; Voth, G. A.; Salvador, P.; Dannenberg, J. J.; Dapprich, S.; Daniels, A. D.; Farkas, Ö.; Foresman, J. B.; Ortiz, J. V.; Cioslowski, J.; Fox, D. J. *Gaussian 09*, Revision E.01; Gaussian Inc.: Wallingford, CT, 2020.

(44) Huang, J.; Rauscher, S.; Nawrocki, G.; Ran, T.; Feig, M.; Groot, B. L. D.; Grubmüller, H.; MacKerell, A. D., Jr. CHARMM36m: An Improved Force Field for Folded and Intrinsically Disordered Proteins. *Nat. Methods* **2017**, *14* (1), 71−73.

(45) Croitoru, A.; Park, S.-J.; Kumar, A.; Lee, J.; Im, W.; MacKerell, A. D., Jr.; Aleksandrov, A. Additive CHARMM36 Force Field for Nonstandard Amino Acids. *J. Chem. Theory Comput.* **2021**, *17* (6), 3554−3570.

(46) Martínez-Rosell, G.; Giorgino, T.; De Fabritiis, G. PlayMolecule ProteinPrepare: A Web Application for Protein Preparation for Molecular Dynamics Simulations. *J. Chem. Inf. Model.* **2017**, *57* (7), 1511−1516.

(47) Brooks, B. R.; Brooks, C. L., III; Mackerell, A. D., Jr.; Nilsson, L.; Petrella, R. J.; Roux, B.; Won, Y.; Archontis, G.; Bartels, C.; Boresch, S.; Caflisch, A.; Caves, L.; Cui, Q.; Dinner, A. R.; Feig, M.; Fischer, S.; Gao, J.; Hodoscek, M.; Im, W.; Kuczera, K.; Lazaridis, T.; Ma, J.; Ovchinnikov, V.; Paci, E.; Pastor, R. W.; Post, C. B.; Pu, J. Z.; Schaefer, M.; Tidor, B.; Venable, R. M.; Woodcock, H. L.; Wu, X.; Yang, W.; York, D. M.; Karplus, M. CHARMM: The Biomolecular Simulation Program. *J. Comput. Chem.* **2009**, *30* (10), 1545−1614.

(48) Jorgensen, W. L.; Chandrasekhar, J.; Madura, J. D.; Impey, R. W.; Klein, M. L. Comparison of Simple Potential Functions for Simulating Liquid Water. *J. Chem. Phys.* **1983**, *79* (2), 926−935.

(49) Neria, E.; Fischer, S.; Karplus, M. Simulation of Activation Free Energies in Molecular Systems. *J. Chem. Phys.* **1996**, *105* (5), 1902−1921.

(50) Durell, S. R.; Brooks, B. R.; Ben-Naim, A. Solvent-Induced Forces between Two Hydrophilic Groups. *J. Phys. Chem. A* **1994**, *98* (8), 2198−2202.

(51) Eastman, P.; Swails, J.; Chodera, J. D.; McGibbon, R. T.; Zhao, Y.; Beauchamp, K. A.; Wang, L.-P.; Simmonett, A. C.; Harrigan, M. P.; Stern, C. D.; Wiewiora, R. P.; Brooks, B. R.; Pande, V. S. OpenMM 7: Rapid Development of High Performance Algorithms for Molecular Dynamics. *PLoS Comput. Biol.* **2017**, *13* (7), No. e1005659.

(52) Darden, T.; York, D.; Pedersen, L. Particle Mesh Ewald: An N·log(N) Method for Ewald Sums in Large Systems. *J. Chem. Phys.* **1993**, *98* (12), 10089.

(53) Essmann, U.; Perera, L.; Berkowitz, M. L.; Darden, T.; Lee, H.; Pedersen, L. G. A Smooth Particle Mesh Ewald Method. *J. Chem. Phys.* **1995**, *103* (19), 8577−8593.

(54) Aldeghi, M.; Bluck, J. P.; Biggin, P. C. Absolute Alchemical Free Energy Calculations for Ligand Binding: A Beginner's Guide. In *Computational Drug Discovery and Design*; Gore, M.; Jagtap, U. B., Eds.; Springer: New York, NY, 2018; pp 199−232.

(55) Wade, A. D.; Bhati, A. P.; Wan, S.; Coveney, P. V. Alchemical Free Energy Estimators and Molecular Dynamics Engines: Accuracy, Precision, and Reproducibility. *J. Chem. Theory Comput.* **2022**, *18* (6), 3972−3987.

(56) Polêto, M. D.; Lemkul, J. A. TUPA: Electric Field Analyses for Molecular Simulations. *J. Comput. Chem.* **2022**, *43* (16), 1113−1119.

https://doi.org/10.1021/acs.biochem.4c00168
Biochemistry 2024, 63, 1783−1794